Naval Surface Warfare Center
Carderock Division
West Bethesda, MD 20817-5700

NSWCCD-50-TR--2001/064 October 2001
Hydromechanics Directorate
Technical Report

High Reynolds Number Boundary Layer Scaling on a Large Hydrofoil (HIFOIL)

by

Wesley H. Brewer and Joel T. Park

NSWCCD-50-TR–2001/08 High Reynolds Number Boundary Layer Scaling on a Large Hydrofoil (HIFOIL) (U)

REPORT DOCUMENTATION PAGE

Form Approved
OMB No. 0704-0188

1. AGENCY USE ONLY *(Leave Blank)*	2. REPORT DATE	3. REPORT TYPE AND DATES COVERED
	October 2001	Final

4. TITLE AND SUBTITLE
High Reynolds Number Boundary Layer Scaling on a Large Hydrofoil (HIFOIL)

5. FUNDING NUMBERS
01-1-5080-209-32

6. AUTHOR(S)
Wesley H. Brewer and Joel T. Park

7. PERFORMING ORGANIZATION NAME(S) AND ADDRESS(ES)
Propulsion and Fluid Systems Department, Code 5400
NSWC, Carderock Division
9500 MacArthur Blvd.
West Bethesda, MD 20817-5700

8. PERFORMING ORGANIZATION REPORT NUMBER
NSWCCD-50-TR-2001/064

9. SPONSORING / MONITORING AGENCY NAME(S) AND ADDRESS(ES)
NSWCCD CODE 5080

10. SPONSORING / MONITORING AGENCY REPORT NUMBER
N/A

11. SUPPLEMENTARY NOTES

12.a DISTRIBUTION / AVAILIBILITY STATEMENT
APPROVED FOR PUBLIC RELEASE

12.b DISTRIBUTION CODE

13. ABSTRACT ***(Maximum 200 words)***

Velocity profiles were measured on a large hydrofoil model to investigate the Reynolds number dependence in a range of $6x10^6$ to $6x10^7$. The friction velocity and skin friction are computed directly from the velocity measurements using the universal velocity-distribution law. The boundary layer profiles are also numerically integrated to yield displacement and momentum thickness, as a function of Reynolds number. Measurements from the foil pressure-side, which is essentially a flat plate, are shown to be in good agreement with skin friction measurements at the same Reynolds numbers. A scaling analysis of the measurements reveals approximately a $1/10^{th}$ power-law relationship of the displacement thickness with Reynolds number.

16. SUBJECT TERMS
Reynolds Number Scaling, HIFOIL, Blasius, Boundary layer, Logarithmic velocity, Skin friction, Drag, Large Cavitation Channel

15. NUMBER OF PAGES
26

16. PRICE CODE

17. SECURITY CLASSIFICATION OF REPORT	18. SECURITY CLASSIFICATION OF THIS PAGE	19. SECURITY CLASSIFICATION OF ABSTRACT	20. LIMITATION OF ABSTRACT
UNCLASSIFIED	UNCLASSIFIED	UNCLASSIFIED	SAME AS REPORT

(THIS PAGE INTENTIONALLY LEFT BLANK)

CONTENTS

ABBREVIATIONS **5**

ABSTRACT **6**

ADMINISTRATIVE INFORMATION **6**

INTRODUCTION **7**

EXPERIMENT **7**

SCALING ANALYSIS **8**

VELOCITY PROFILES 9

LOGARITHMIC-LINEAR REGRESSION 9

SKIN FRICTION 11

CHARACTERISTIC NUMBERS 11

Displacement Thickness 12
Momentum Thickness 12
Shape Factor 14

SECTION DRAG 14

CONCLUSIONS **15**

ACKNOWLEDGEMENTS **16**

REFERENCES **31**

TABLES

Table 1. Distance (in mm) that data is shifted such that B = 5.5 11
Table 2. Power-law constants for computing δ^* on foil pressure-side 13

FIGURES

Figure 1. William B. Morgan Large Cavitation Channel 17
Figure 2. HIFOIL Geometry showing where LDV data was analyzed. 17
Figure 3. HIFOIL Geometry showing trailing edge detail. 17
Figure 4. Pressure-side mean axial velocity profiles. 18
Figure 5. Mean axial velocity profile at x/c = 1.000 pressure side (normalized by U). 20
Figure 6. Pressure-side inner-variable velocity profiles. 21
Figure 7. Suction-side mean velocity profiles. 23
Figure 8. Suction-side inner-variable velocity profiles. 24
Figure 9. Local skin-friction coefficient computed from pressure-side velocity profiles. 26
Figure 10. Displacement and momentum thickness versus Reynolds number. 27
Figure 11. Re_θ versus Re_x 28
Figure 12. Shape Factor as a function of Reynolds number 28
Figure 13. Pressure-side mean axial velocity profiles showing shape similarity. 29
Figure 14. LDV wake measurements taken at x/c = 1.028 30
Figure 15. Reynolds number dependence of drag coefficient. 30

NOMENCLATURE

A	Slope for u^+ vs. y^+. Taken here as 2.5 (1/0.4).
B	y-intercept for u^+ vs. y^+
c	Chord length
C	Constant for power-law curve-fit, $\frac{\delta^*}{c} = C \times Re^{-1/n}$
C_D	Drag coefficient of section, $\frac{\text{Drag}}{\frac{1}{2}\rho V_{rel}^2 C}$
C_{DP}	Portion of drag coefficient due to pressure drag
C_{Df}	Portion of drag coefficient due to friction drag
C_f	Skin friction coefficient, $\frac{\tau_o}{\frac{1}{2}\rho U^2}$
c_f	Local skin friction coefficient
d	y-intercept for u vs. $\ln y$
H	Shape factor, $= \frac{\delta^*}{\theta}$
k^+	Hydraulic smoothness, $= \frac{ku^*}{\nu}$
k	Surface roughness (in *meters*)
l	Arbitrary characteristic length scale
m	Slope of logarithmic-linear relationship u vs. $\ln y$
n	Power for power-law curve-fit, $\frac{\delta^*}{c} = C \times Re^{-1/n}$
Re	Reynolds number based on chord, $= \frac{Uc}{\nu}$
Re_l	Reynolds number, $= \frac{Ul}{\nu}$, where l can be either c, x, or θ.
u	Mean axial velocity $u(y)$
u^*	Friction velocity, $= \sqrt{\frac{\lvert\tau_o\rvert}{\rho}}$

u^+	Non-dimensional mean velocity in inner variables, $=\frac{u}{u^*}$
U	Reference velocity
U_e	Velocity at edge of boundary layer, where y = δ
x	Distance from leading edge of foil to measurement location.
y	Distance from wall (in meters)
y^+	Inner variable, $=\frac{yu^*}{\nu}$
z	Same as y, vertical distance from wall
z_o	Location of foil surface
δ	Boundary layer thickness, distance from wall where $u(y) = 0.99U_\infty$
δ^*	Displacement thickness, $\delta^* = \int_{y=0}^{y=\delta} (1-\frac{u}{U_e})dy$
θ	Momentum thickness, $\theta = \int_{y=0}^{y=\delta} (1-\frac{u}{U_e})\frac{u}{U_e}dy$
θ_∞	Momentum thickness computed far downstream of foil
ρ	Mass density
τ_o	Wall sheer stress
ν	Kinematic viscosity

ABBREVIATIONS

HIFOIL	High Reynolds number Foil
LCC	Large Cavitation Channel
LDV	Laser Doppler Velocimetry
NACA	National Advisory Committee for Aeronautics
NSWCCD	Naval Surface Warfare Center, Carderock Division
ONR	Office of Naval Research

ABSTRACT

Velocity profiles were measured on a large hydrofoil model to investigate the Reynolds number dependence in a range of $6x10^6$ to $6x10^7$. The friction velocity and skin friction are computed directly from the velocity measurements using the universal velocity-distribution law. The boundary layer profiles are also numerically integrated to yield displacement and momentum thickness, as a function of Reynolds number. Measurements from the foil pressure-side, which is essentially a flat plate, are shown to be in good agreement with skin friction measurements at the same Reynolds numbers. A scaling analysis of the measurements reveals approximately a $1/10^{th}$ power-law relationship of the displacement thickness with Reynolds number.

ADMINISTRATIVE INFORMATION

The Office of Naval Research funded the University of Michigan to perform the experiments under contract numbers N00014-99-1-0341 and N00014-99-1-0856. Jude Brown, of Code 508, sponsored the Reynolds number scaling analysis of the data presented in this report. The scaling analysis was conducted by the Naval Surface Warfare Center, Carderock Division (NSWCCD), Hydromechanics Directorate, Propulsion and Fluid Systems Department (Code 5400) under work unit number 01-1-5080-209-32.

INTRODUCTION

In response to an Office of Naval Research (ONR) request to address basic research in the area of High Reynolds number flows, a three-phase experimental effort was undertaken at the Large Cavitation Channel by the University of Michigan. The overall goal of this experimental effort was to increase our knowledge of turbulence in high Reynolds number flows [1]. The results of this research will help to improve prediction, analysis, and control of full-scale turbulent flows about ships and submarines.

The results presented herein seek to reveal findings from the phase I experiment, specifically relating to the scaling of model-scale to full-scale boundary layers. Not until recently, have facilities been capable of testing near full-scale Reynolds number ranges. Therefore, little to no experimental data exist for boundary layer measurements at Reynolds numbers in the 10^7 range. This report reveals the Reynolds number relationship to the boundary layer at chord Reynolds numbers range from $6x10^6$ to $6x10^7$.

Blasius' $1/5^{th}$ power-law relationship for displacement and momentum thickness (deduced from the $1/7^{th}$-power velocity distribution law) only gives good agreement with experimental data up to Reynolds numbers of 10^5. This report shows experimental evidence for a $1/10^{th}$ power-law relationship for the tested Reynolds number range.

EXPERIMENT

Experiments were performed at the William B. Morgan Large Cavitation Channel (LCC) in Memphis, TN. As illustrated in Figure 1, the LCC is a closed-loop re-circulating water channel. It has a 3-meter square test section, and is about 13 meters long. The channel has a speed range from 0.5 to 18 m/s. The ambient pressure in the test section can be varied from 3.5 to 414 kPa. Etter and Wilson [2] have discussed the Large Cavitation Channel in detail. Moreover, Blanton [3] describes measurement capabilities and provides an uncertainty analysis of velocity and pressure measurements taken at the LCC.

The test device was a foil, named "HIFOIL" (**Hi**gh Reynolds Number **Foil**), which is typical of a full-scale section of a propeller. The foil is a modification to a NACA 16 thickness form with $a = 0.8$ mean-line camber. The aft 3% of the suction-side is modified to intentionally separate the flow, giving the foil an "anti-singing" characteristic. The pressure side of the foil is completely flat aft of $x/c = 0.28$. Figure 2 shows the geometry of the foil, and Figure 3 shows the trailing edge in detail. HIFOIL has a chord length of *2.134 meters* and a maximum thickness of

0.171 meters. The surface roughness is less than *0.25μm*, which corresponds to a maximum hydraulic smoothness $k^+ = 0.2$ *at 18.3 m/s*. At the highest speed, 18.3 m/s, the foil generated an estimated lift force of 670 kN (150,000 lbf) [4]. The foil was placed at a *zero* angle of attack.

Laser Doppler Velocimetry (LDV) measurements were taken on the pressure side at four x/c locations: 0.930, 0.957, 0.979, and 1.0. On the suction side, stations were analyzed at three x/c locations: 0.930, 0.957, and 0.979. In addition, a station in the wake at $x/c = 1.028$ was also investigated. The experiment was performed at four different speeds: 3, 6, 12, and 18 m/s. These correspond to nominal[1] Reynolds numbers of 9.0×10^6, 1.9×10^7, 3.7×10^7, and 5.6×10^7 respectively. The foil was allowed to naturally transition from laminar to turbulent flow. This fact has introduced some small scatter in the data shown, because the transition location probably changes with speed. This scatter is most evident in the 3 and 6 m/s data. Future experiments plan to incorporate trip-wires to force transition on the foil at a fixed location. Bourgoyne [4] describes this experiment in detail and presents turbulence measurements for the current data.

SCALING ANALYSIS

The pressure-side of the foil is assumed to have the same flow physics as flat-plate flow. This hypothesis was verified three ways: (1) verifying the pressure gradient is zero on the pressure-side of the foil, (2) comparing local skin friction coefficients with flat-plate theory, and (3) verifying that profiles taken at different x/c locations exhibit shape factor similarity. Bourgoyne [4] measured the pressure distribution on both the pressure and suction side of HIFOIL during phase II of the experiment. The pressure-side results do indeed show a negligible pressure gradient in the trailing edge region, where the velocity profiles are measured. Local skin friction and shape factor correlations will be given in the Skin Friction and Characteristic Numbers sections, respectively.

To investigate the Reynolds number dependence of the boundary layer, the velocity profiles are numerically integrated to compute displacement and momentum thickness and the shape factor. Also, the profiles are plotted in inner-variable coordinates, u^+ vs. y^+, which clearly show the effect of Reynolds number on the profiles. The skin friction coefficients presented are not measured, but instead are inferred from the velocity measurements. The Logarithmic-linear Regression section explains how this analysis was done.

[1] The temperature of throughout the experiment varied from 22 to 40 degrees Celsius (71.5 to 104.2 degrees Fahrenheit), causing the Reynolds number to vary for a fixed speed. Although for the data given here, the Reynolds number remained relatively constant for each condition, and should be taken as those given above.

VELOCITY PROFILES

As shown in Figure 4, the HIFOIL boundary layer profiles show negligible variation with Reynolds number, when looking at mean velocity profiles. Normalizing the profiles with the edge velocity, U_e, instead of U_∞, reveals a small variation in the boundary layer region and highlights that the changes are occurring in the overlap layer. For example, compare Figure 4d and Figure 5. The changes become obvious when the data are normalized by the friction velocity, u^*. Figure 6 shows the experimental measurements from the *pressure-side* plotted in inner variable coordinates. The next section shows the method used to shift and scale the boundary layer data, such that it can be plotted in u^+, y^+ coordinates. In all the velocity profile figures, Spalding's [5] law of the wall model is shown. Spalding's single formula for the law of the wall [5] is given as:

$$y^+ = u^+ + e^{-\kappa B}\left[e^{-\kappa u^+} - 1 - \kappa u^+ - \frac{(\kappa u^+)^2}{2} - \frac{(\kappa u^+)^3}{6}\right] \qquad (1)$$

where κ is a dimensionless constant, taken here as 0.40. u^+ and y^+ are inner-variable coordinates. All profiles collapse to Spalding's law of the wall model, though each profile was shifted independently.

Figure 7 shows axial mean velocity profiles in outer variables for the *suction-side* of the foil, taken at x/c = 0.930, 0.958, and 0.979, respectively. Figure 8 shows the same data plotted in inner-variable coordinates. This data was more difficult to shift correctly, because only a few points were in the logarithmic region. On the suction-side, separation appears to occur just downstream of the $x/c = 0.979$ profile. The adverse pressure gradient tends to shift the data above the logarithmic law [8]. In the $x/c = 0.979$ profile (Figure 8c), the data has not been shifted due to the difficulty in determining the logarithmic region. Note that the *x/c = 0.979* profile was just downtream of the "knuckle", as shown in Figure 3.

LOGARITHMIC-LINEAR REGRESSION

This section explains how the data is shifted to fit the universal velocity-distribution law, and how u^* and C_f are computed. The logarithmic velocity-distribution law states a linear-logarithmic relationship between the velocity and the distance from the wall as such:

$$u^+ = A \ln y^+ + B \qquad (2)$$

where typically $A = 2.5$ and $B = 5.5$. Here,

$$u^+ = \frac{u}{u^*} \text{ and } y^+ = \frac{yu^*}{\nu} \text{ where } u^* = \sqrt{\frac{|\tau_o|}{\rho}} \tag{3}$$

u^* is the friction velocity, and is a measure of the turbulent eddying in the outer boundary layer [6]. Also, τ_o is the shear stress at the wall and ρ is the density of the fluid. Thus, using the previous equations, a new dimensional form of the universal velocity-distribution law, is:

$$u = Au^* \ln\left(\frac{y}{l}\right) + Au^* \ln\left(\frac{lu^*}{\nu}\right) + Bu^* \tag{4}$$

Let $y = z - z_o$, where z_o represents the location of the wall surface. Since the precise location of the wall surface is not known, it must be determined iteratively. Furthermore, define $m = Au^*$ and $d = Au^* \ln\left(\frac{lu^*}{\nu}\right) + Bu^*$ as shown above, which leaves

$$\boxed{u = m \ln\left(\frac{z - z_o}{l}\right) + d} \tag{5}$$

Here u and z are given (in *m/s* and *m* respectively) from the experiment, l is an arbitrary scale length (taken here as *one*), and m and d are determined from a linear regression analysis of the linear-log region of the boundary layer. The z_o is determined iteratively such that B=*5.5,* now given by

$$B = \frac{d}{u^*} - A \ln \frac{u^*}{\nu} \tag{6}$$

The friction velocity can now conveniently be computed from:

$$u^* = \frac{m}{A} \tag{7}$$

Also, u^+ and y^+ are computed from the friction velocity, u^*, in addition to the local skin friction coefficient, which is computed as:

$$c_f = \tau_o / (\rho U^2 / 2) = (u^* / U)^2 \tag{8}$$

Table 1 shows the distance in *mm* that each velocity profile was shifted. For most cases, the shift was smaller than the probe diameter (*0.2mm*) of the LDV.

Table 1. Distance (in mm) that data is shifted such that B = 5.5

	x/c	U (m/s)	3	6	12	18
Pressure	**0.930**		0.37	0.28	0.18	0.47
	0.958		0.38	0.08	0.17	0.30
	0.979		0.40	0.03	0.05	0.17
	1.000		-0.09	-0.03	-0.08	-0.07
Suction	**0.930**		-0.15	0.11	-0.02	-0.31
	0.958		-0.05	-0.23	-0.29	0.00

SKIN FRICTION

Various skin-friction formulas are given in Schlichting [6], each tending to work well for a specified Reynolds number range. Three are applicable to Reynolds number range of the HIFOIL experiment:

Blasius Theory	$c_f = 0.0592(Re_x)^{-1/5}$	$5\text{x}10^5 < Re_x < 10^7$	(9)
Prandtl-Schlichting	$c_f = 2\log(Re_x - 0.65)^{-2.3}$	$10^7 < Re_x < 10^9$	(10)
Schultz-Grunow	$c_f = 0.0592(Re_x)^{-1/5}$	$10^6 < Re_x < 10^8$	(11)

Figure 9 shows the local skin friction coefficient from the foil *pressure-side* compared with the previous formulas. The HIFOIL experimental data is shown to lie below the theoretical models. This is most likely due to a difference in transition locations between experiment and theory. In fact, the *Prandtl-Schlichting* formula (for total skin friction) even includes a correction for transition location. Kempf [6] achieved experimental total-skin-friction coefficients up to $Re = 5\text{x}10^8$. His data tended to lie between midway between Equations (10) and (11) for the Reynolds number range in this experiment.

CHARACTERISTIC NUMBERS

To show Reynolds number effects, the displacement thickness, momentum thickness and shape factors are computed.

Displacement Thickness

The displacement thickness is a characteristic number representing the distance streamlines are displaced due to the presence of the boundary layer, and is defined as:

$$\delta^* = \int_{y=0}^{y=\delta}\left(1-\frac{u}{U_e}\right)dy \approx \sum_{y=0}^{y=\delta}\left(1-\frac{u}{U_e}\right)\Delta y \tag{12}$$

It was integrated numerically using the Trapezoidal rule. Experimental measurements taken with the LDV yielded average minimum y^+ values[2] of about 80. To accurately compute the displacement thickness, Spalding's wall model, Equation (1), was used for $0 < y^+ < 80$. Thus,

$$\delta^* \approx \underbrace{\sum_{y=0}^{y=y_{\min}}\left(1-\frac{u}{U_e}\right)\Delta y}_{Spalding} + \underbrace{\sum_{y=y_{\min}}^{y=\delta}\left(1-\frac{u}{U_e}\right)\Delta y}_{Experiment} \tag{13}$$

where y_{min} corresponds to the distance of the measurement closest to the wall.

Momentum Thickness

The momentum thickness, like the displacement thickness, is a characteristic number that gives a measure of the loss of momentum in the boundary layer, owing to the frictional losses caused by the fluid interaction with the wall. A similar computation is performed to compute the momentum thickness, defined as:

$$\theta = \int_{y=0}^{y=\delta}\left(1-\frac{u}{U_e}\right)\frac{u}{U_e}dy \approx \sum_{y=0}^{y=\delta}\left(1-\frac{u}{U_e}\right)\frac{u}{U_e}\Delta y \tag{14}$$

Similarly, this can be written as

$$\theta \approx \underbrace{\sum_{y=0}^{y=y_{\min}}\left(1-\frac{u}{U_e}\right)\frac{u}{U_e}\Delta y}_{Spalding} + \underbrace{\sum_{y=y_{\min}}^{y=\delta}\left(1-\frac{u}{U_e}\right)\frac{u}{U_e}\Delta y}_{Experiment} \tag{15}$$

[2] The distance to the wall was limited to the accuracy of the laser. The LDV has a probe volume of $0.2mm$ which corresponds to wall coordinates between 60 and 160.

Figure 10a shows the results of this research for the *pressure-side* data. Notice the data scatter for the four different Reynolds numbers. The 3 m/s ($Re = 9x10^6$) shows little data scatter, and the resulting displacement thickness is less than the other cases. The transition location possibly is further aft in the lowest Reynolds number case, causing "thinner" results for the lower Reynolds number case. The 6 m/s data ($Re = 19x10^6$) exhibits more data scatter, which can be attributed to transition location uncertainty. On the other hand, the high Reynolds number case, 18 m/s ($Re = 5.6x10^7$) shows to be fully turbulent.

Figure 10b indicates the *suction-side* displacement and momentum thickness as a function of Reynolds number. The data does not collapse as in Figure 10a, due to the changing pressure gradient in the trailing edge region.

The Reynolds number is computed based on the momentum thickness. This is defined as:

$$Re_\theta = \frac{U_e \theta}{\nu} \tag{16}$$

Figure 11 shows a log-log relationship between Re_θ and Re_x.

A power-law curve fit of the displacement thickness versus Reynolds number for the *pressure-side* data is shown in Table 2. The average computed in Table 2 does not include the data in the wake ($x/c = 1.028$). Here, C and n are the constants in the following expression:

$$\frac{\delta^*}{c} = C \times Re^{-1/n} \tag{17}$$

Table 2. Power-law constants for computing δ^* on foil pressure-side.

x/c	*C*	*n*
Blasius	0.046	5
0.930	0.0088	10.6
0.956	0.0106	9.5
0.978	0.0119	8.9
1.000	0.0109	9.2
1.028	0.0272	9.8
Average (*excluding x/c = 1.028*)	**0.0106**	**9.6**

Shape Factor

The *shape factor* is a dimensionless characteristic number quantifying the velocity profile shape, and is given here as:

$$H = \frac{\delta^*}{\theta} \tag{18}$$

The shape factor is heavily dependent on the external pressure gradient [6]. Hinze [7] reports a dependence of shape factor on Reynolds number, but the variation is small for high Reynolds numbers. Based on Blasius' theory [6], the shape factor for the flat plate is independent of Reynolds number and has a value of *1.278*. Figure 12 shows the shape factor's dependence on Reynolds number for both the pressure and suction-side experimental data. As is expected the *pressure-side* data shows little dependence on the Reynolds number and collapses on the theoretical prediction. This again is verified in Figure 13 where four different profiles collapse, each profile being scaled by its edge velocity. This shows that the pressure-side of HIFOIL does produce very similar flow physics to that of a flat plate. On the other hand, the *suction-side* data tends to change drastically depending on the *x/c* location where the data were measured. The *x/c* = *0.978* shape factor is much higher than the two cuts at *x/c* = *0.930* and *x/c* = *0.958*, owing to the fact that this profile is just downstream of the knuckle, as shown in Figure 3. This indicates the strong dependence on the external pressure gradient that was alluded to earlier. Previous research suggests separation occurs at a value of H of about 4.0 [8].

SECTION DRAG

The drag on the hydrofoil is directly related to the momentum deficit in its wake. This can be expressed as:

$$C_D = 2\frac{\theta_\infty}{c} \tag{19}$$

where θ_∞ is the momentum thickness at a distance downstream of the body, computed from Equation (6). Figure 14 shows the LDV measurements taken at *x/c* = 1.028. These data have been normalized by the edge velocity. Because of the nature of the separated flow from the blunt trailing edge, the data in the wake exhibit higher turbulence for the suction side of the foil ($y > 0$), and thus shows more scatter in the data.

In order to investigate Reynolds number scaling from the measured drag, the base drag must be subtracted from the total drag. For this case, C_f was estimated using:

$$\frac{1}{2}C_f(\mathrm{Re}) = 0.074 \times Re^{-1/5} \tag{20}$$

where the ½ accounts for just one side of the foil. Hence, to obtain the total skin friction for both sides of the foil, Equation (20) is doubled. Unless the separation point moves, pressure drag should be a constant value (independent of Reynolds number). Hence, an average value of C_{DP}^{AVG} was used to estimate the portion of drag due to pressure loss, as such:

$$C_{DP}^{AVG} = C_D - \frac{1}{3}(C_f(1.9x10^7) + C_f(3.7x10^7) + C_f(5.6x10^7)) \tag{21}$$

C_{DP}^{AVG} here is computed to be 0.0054 and is subtracted from the drag coefficient computed in Equation (8) to compute C_{Df}, the portion of drag due to friction:

$$C_{Df} = C_D - C_{DP}^{AVG} \tag{22}$$

Figure 15 shows the results of this study. Most of the pressure drag is due to the flow separation on the suction-side of the foil. It is interesting to note, that when the pressure drag is subtracted from the total drag, the resulting power, n, is 9.6, which is almost identical to the power previously shown in the boundary layer studies. Shen developed a theory for more accurately predicting n, for a given Reynolds number ratio. For the Reynolds number range presented here, Shen's theory predicts $n = 9.5$ [9]. This is almost exactly what the experiment shows in Table 2.

CONCLUSIONS

Boundary layer data, measured in a Reynolds number range from $6x10^6$ to $6x10^7$, have shown to exhibit a $1/10^{th}$ power-law relationship with Reynolds number. Skin friction, inferred from measurements taken on the pressure-side of the foil, is in good agreement with existing data taken at the same Reynolds number. Displacement and momentum thickness are computed by numerically integrating the velocity profiles. The shape factor is also computed and shows shape similarity for the four locations on the pressure-side of the foil. The momentum thickness in the wake is used to compute the drag coefficient on the foil. Frictional drag is deduced from the total

drag and is shown to exhibit similar trends as the measurements taken on the flat/pressure side of the foil. Future experiments should be performed at higher Reynolds number ranges on flat-plate flow to show a higher-order correlation of the boundary layer's dependence on Reynolds number. Moreover, more analysis should be performed on the suction-side data to investigate high Reynolds number effects of separated flows.

ACKNOWLEDGEMENTS

The authors also gratefully appreciate the funding that was given by Jude Brown for this further analysis of the data. Much appreciation goes to Stuart Jessup, Young Shen, and C.I. Yang for all their advice, support, and numerous discussions on the subject of Reynolds number scaling. Also, thanks to Steve Ceccio, David Dowling, and Dwayne Bourgoyne of University of Michigan for allowing us to use the experimental data. Thanks to Mike Cutbirth and the guys at the LCC for all their hard work on this experiment. Also, thanks to David Whitfield, Lafe Taylor, Ramesh Pankajakshan, Kidambi Sreenivas, Brent Mitchell, and Min-Yee Jiang, of Mississippi State University, for helping to support the computational simulation of HIFOIL.

Soli Deo Gloria.

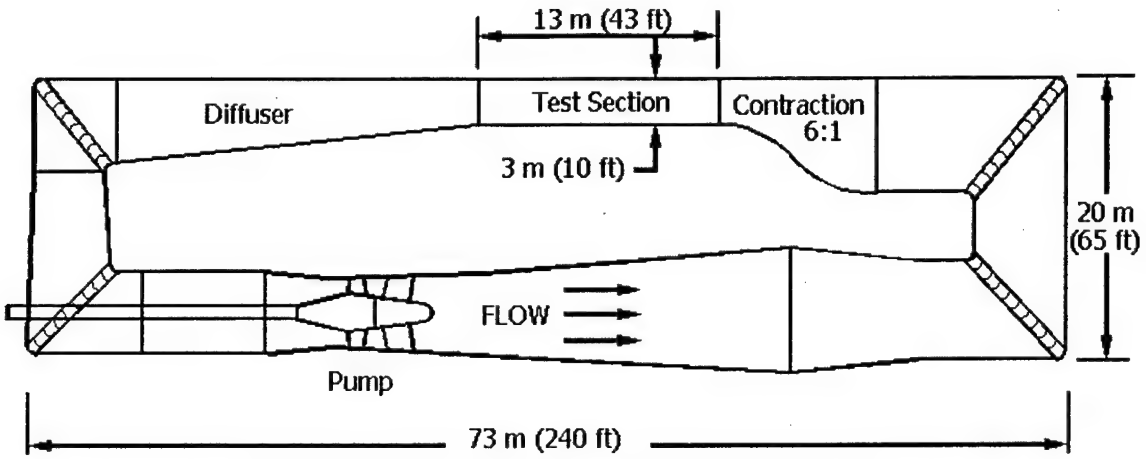

Figure 1. William B. Morgan Large Cavitation Channel

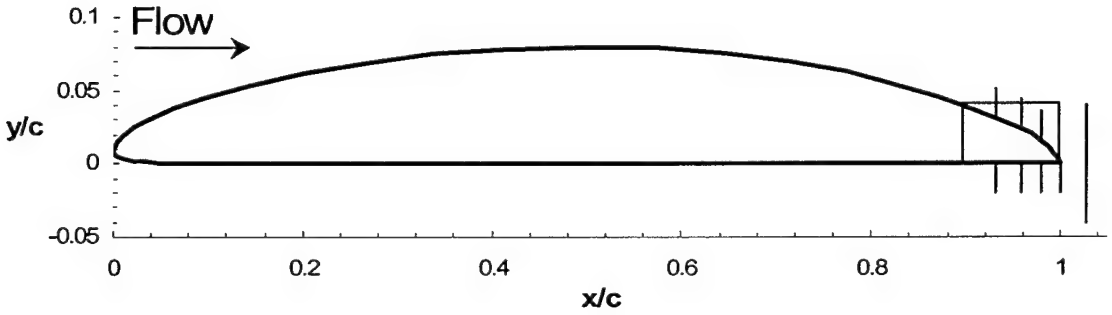

Figure 2. HIFOIL Geometry showing where LDV data was analyzed.

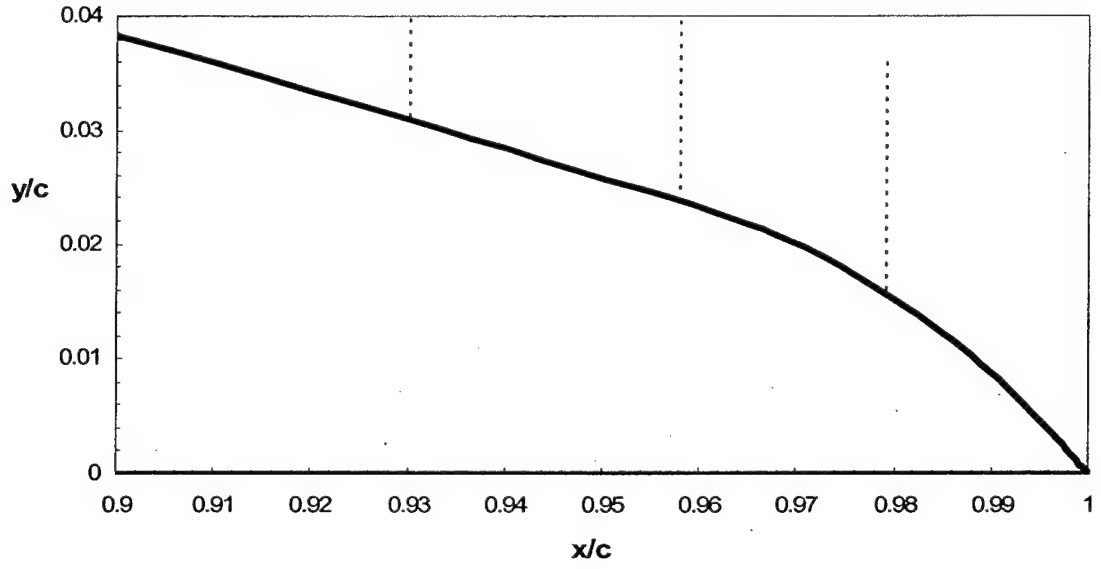

Figure 3. HIFOIL Geometry showing trailing edge detail.

Figure 4. Pressure-side mean axial velocity profiles.

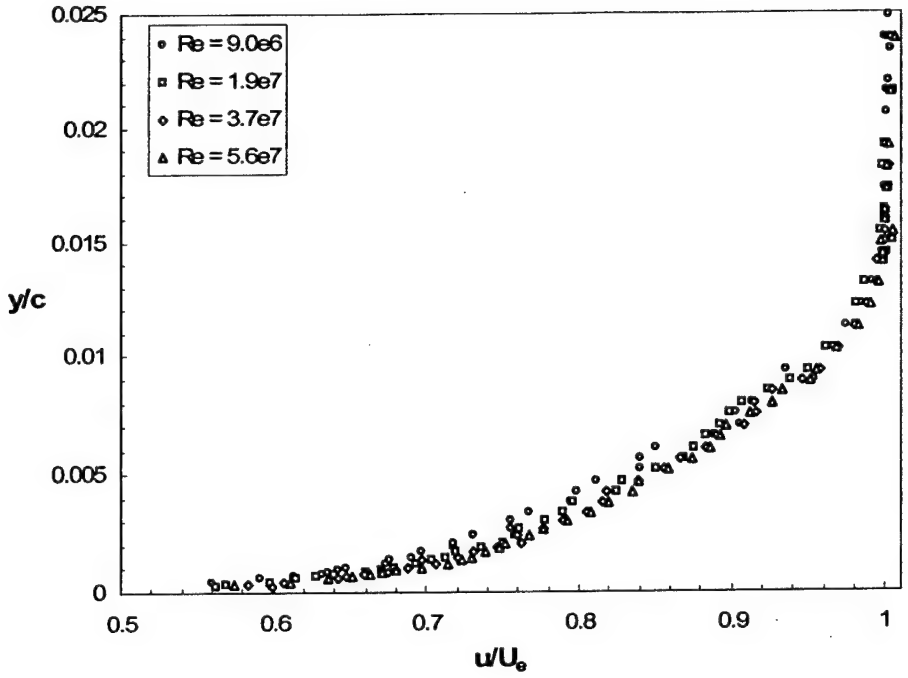

a. x/c = 0.930 pressure side.

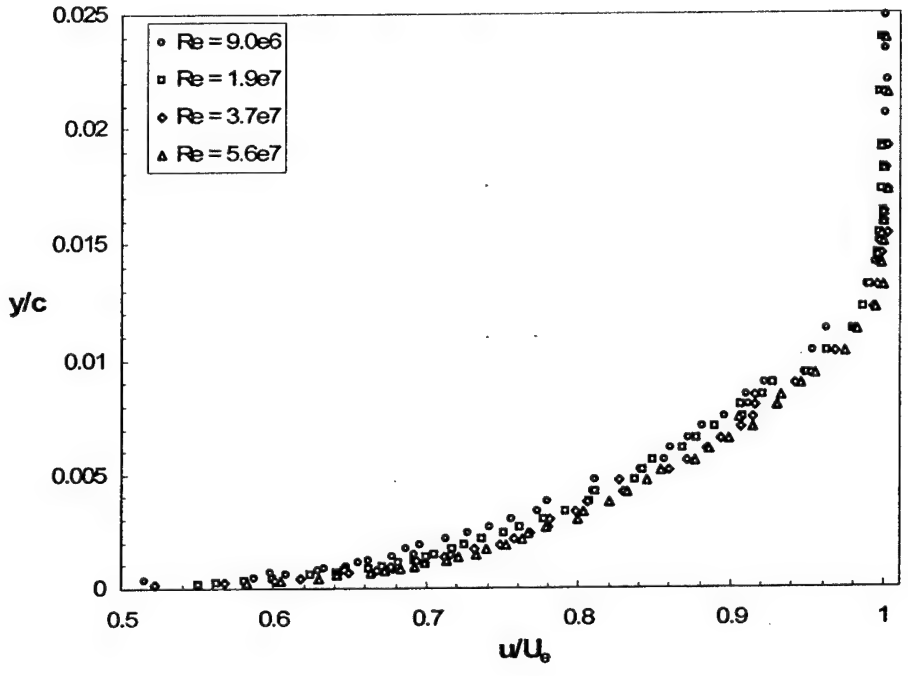

b. x/c = 0.958 pressure side.

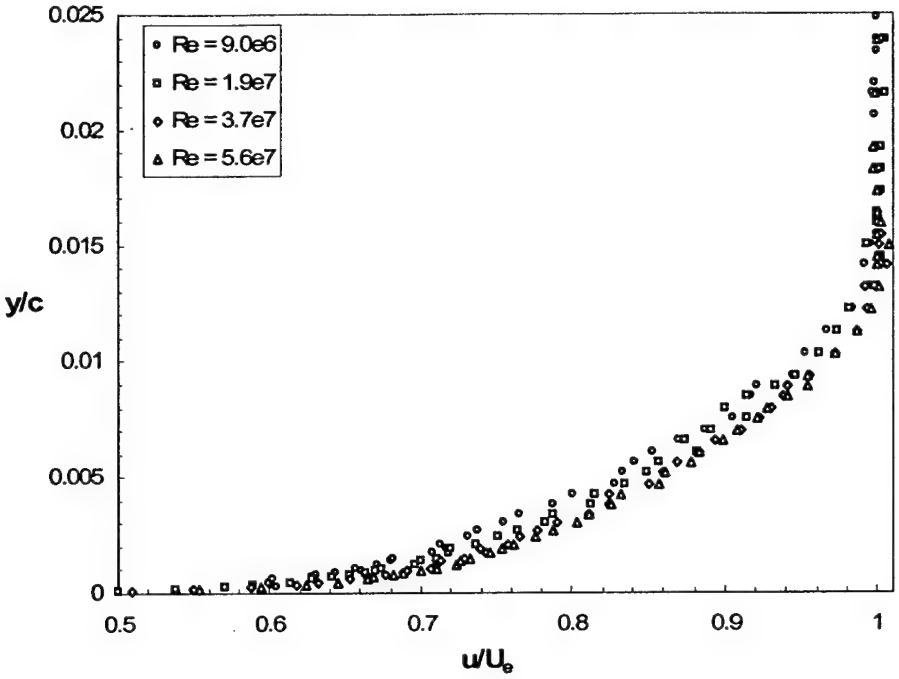

c. x/c = 0.979 pressure side.

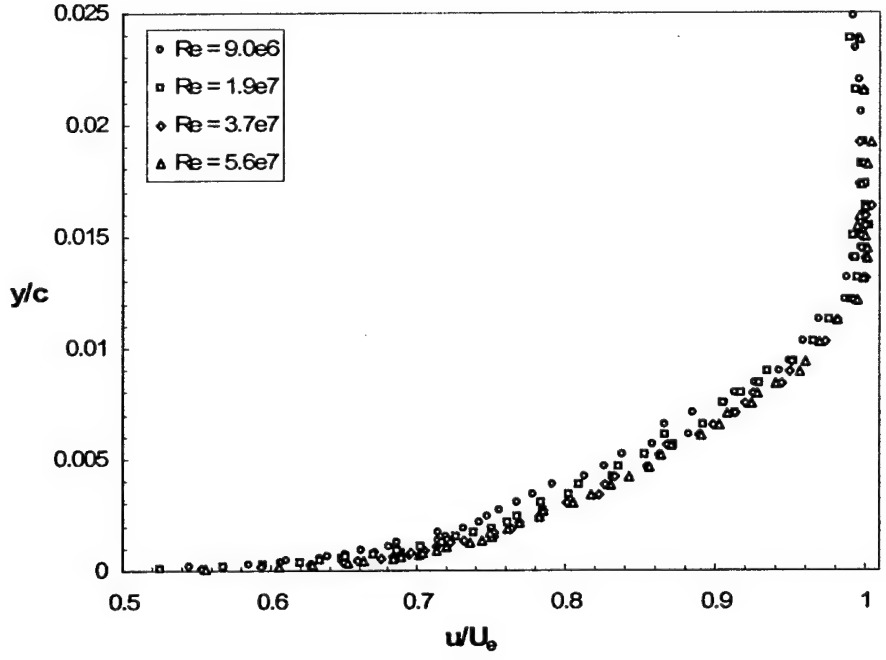

d. x/c = 1.0 pressure side.

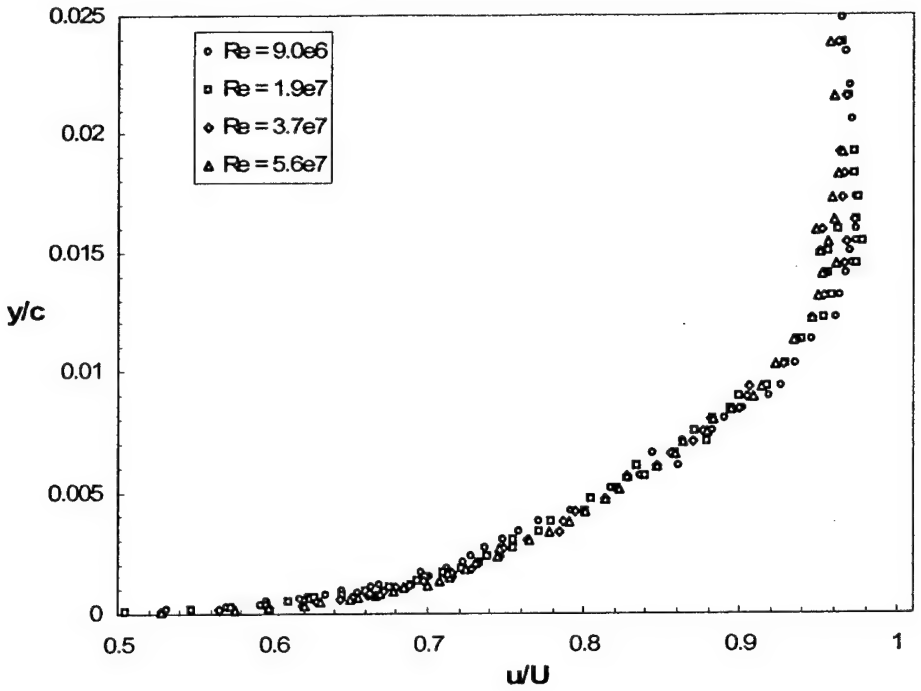

Figure 5. Mean axial velocity profile at x/c = 1.000 pressure side (normalized by *U*).

Figure 6. Pressure-side inner-variable velocity profiles.

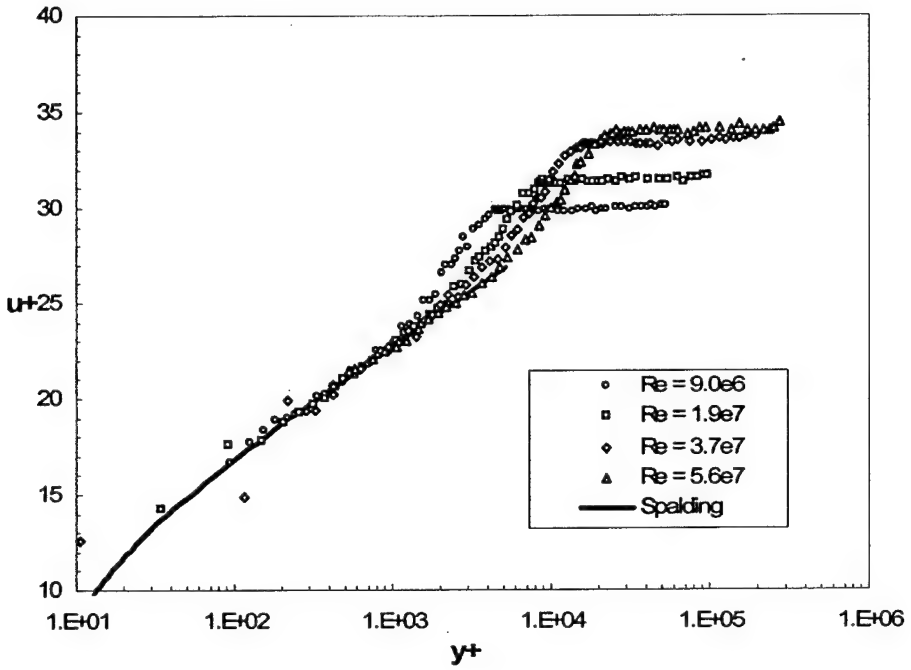

a. x/c = 0.930 pressure side.

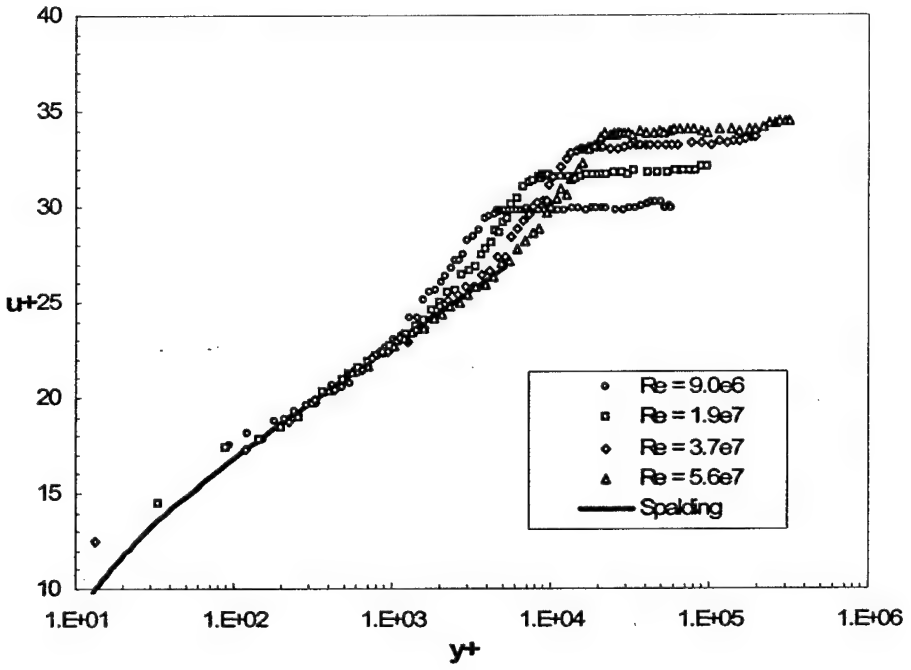

b. x/c = 0.958 pressure side.

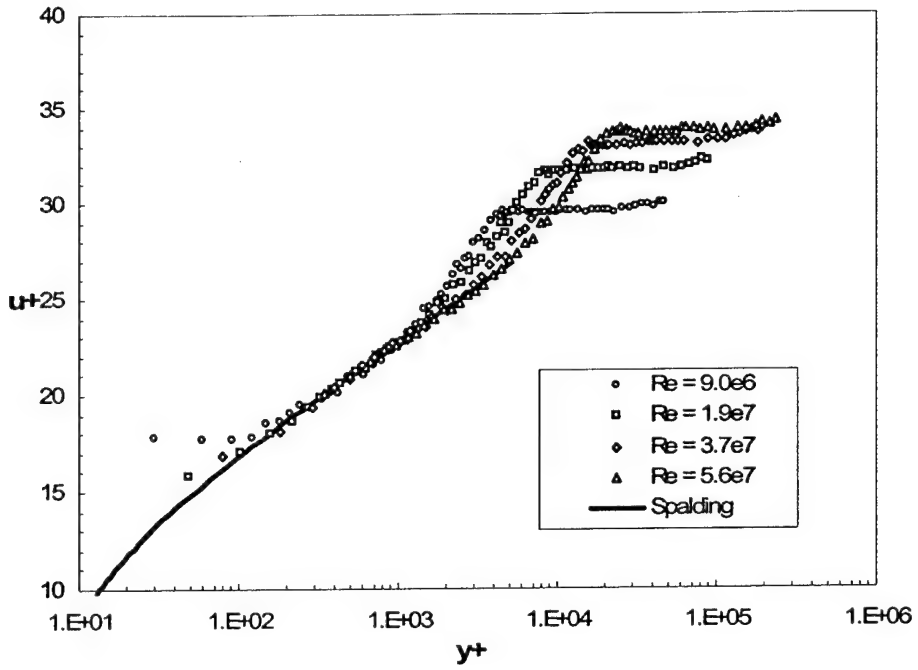

c. x/c = 0.979 pressure side.

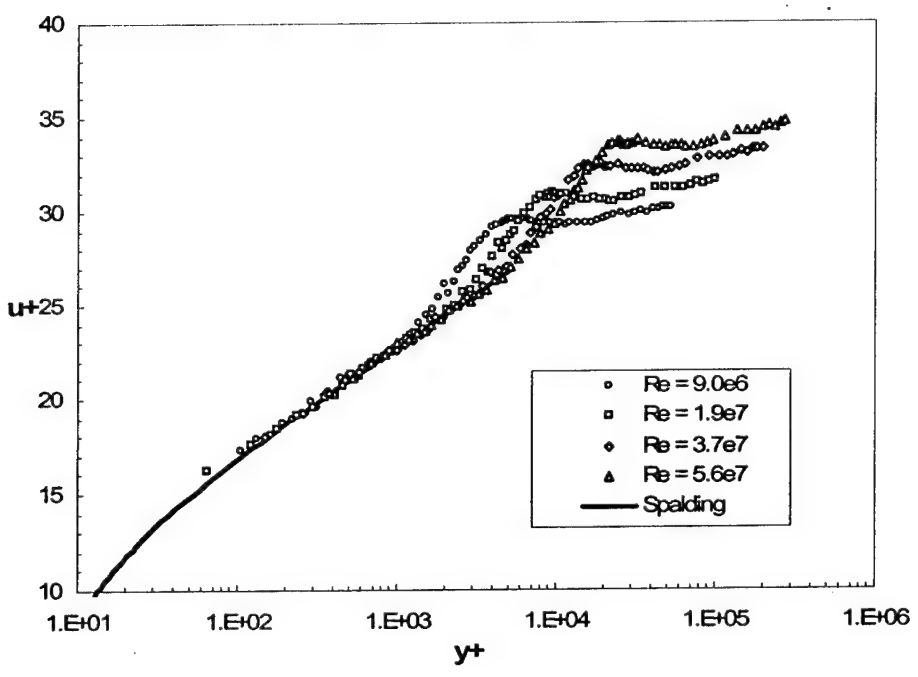

d. x/c = 1.0 pressure side.

Figure 7. Suction-side mean velocity profiles.

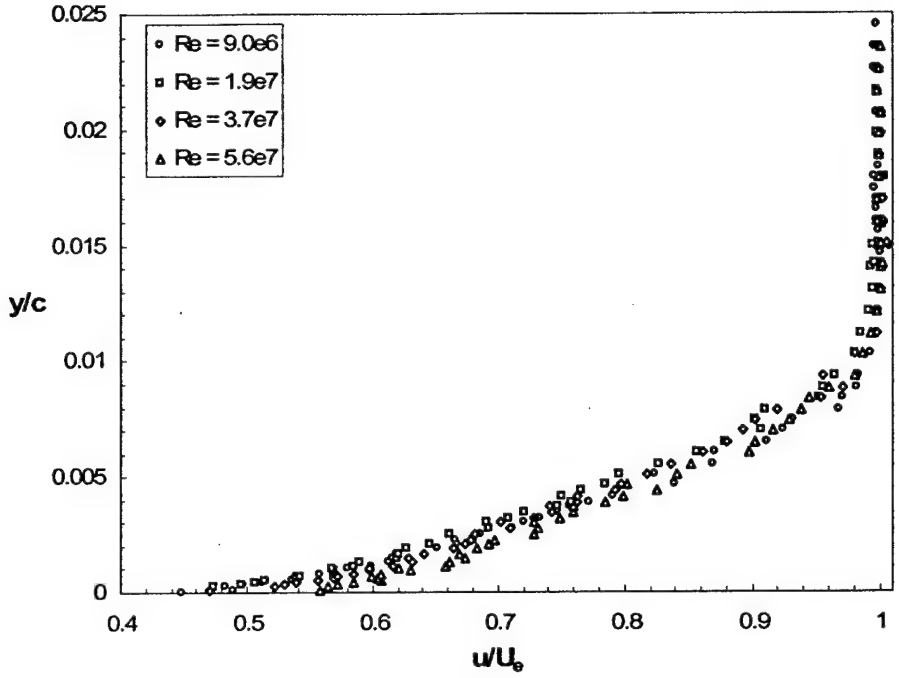

a. x/c = 0.930 suction side.

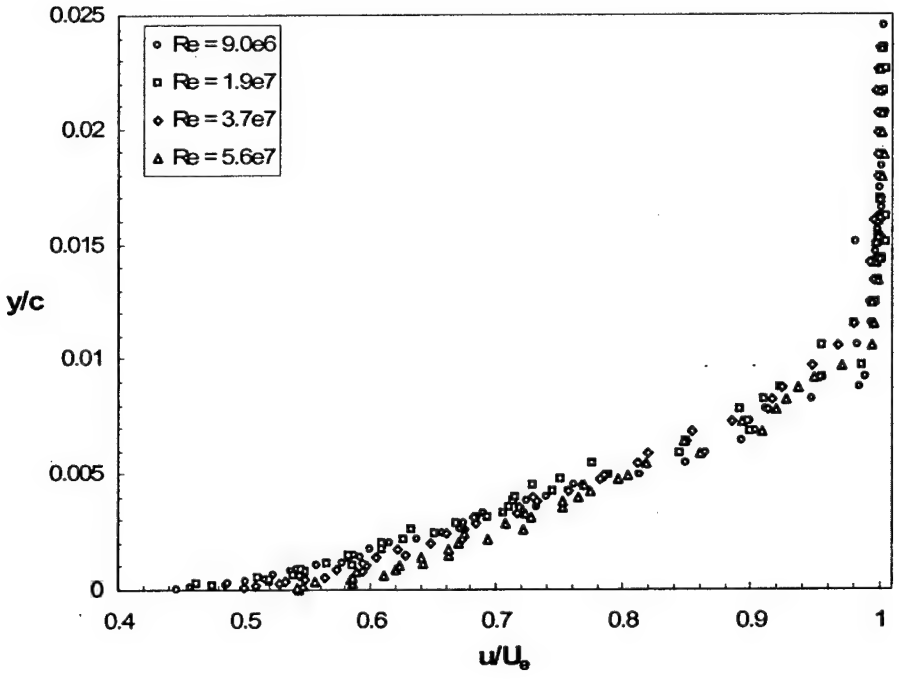

b. x/c = 0.958 suction side.

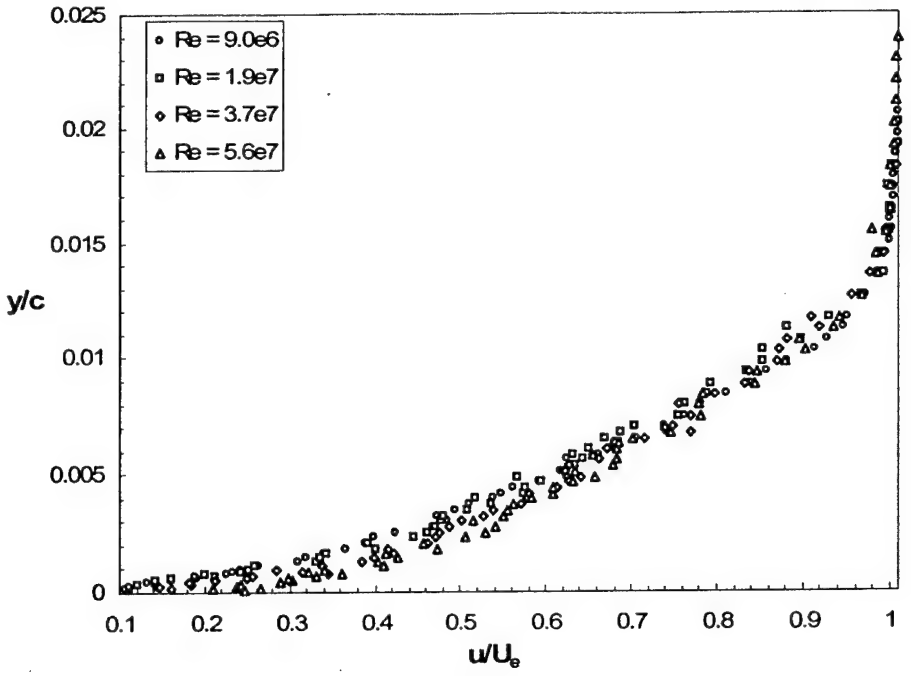

c. x/c = 0.979 suction side.

Figure 8. Suction-side inner-variable velocity profiles.

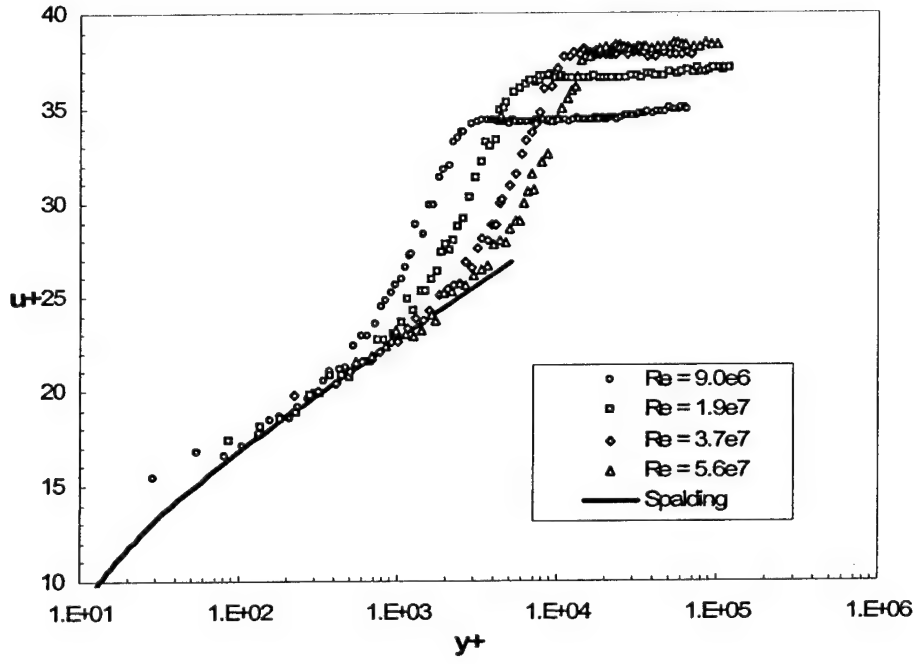

a. x/c = 0.930 suction side.

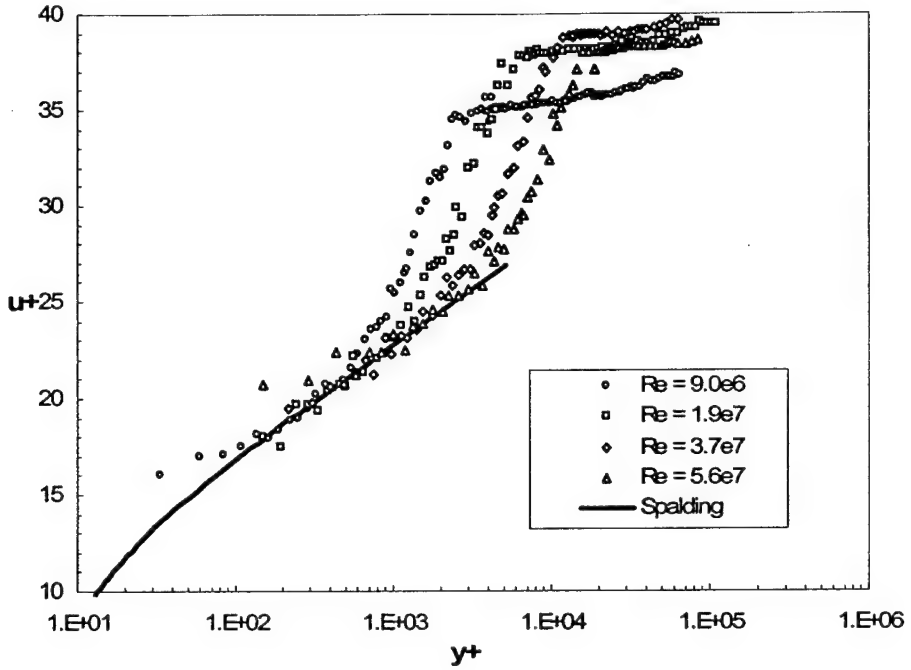

b. x/c = 0.958 suction side.

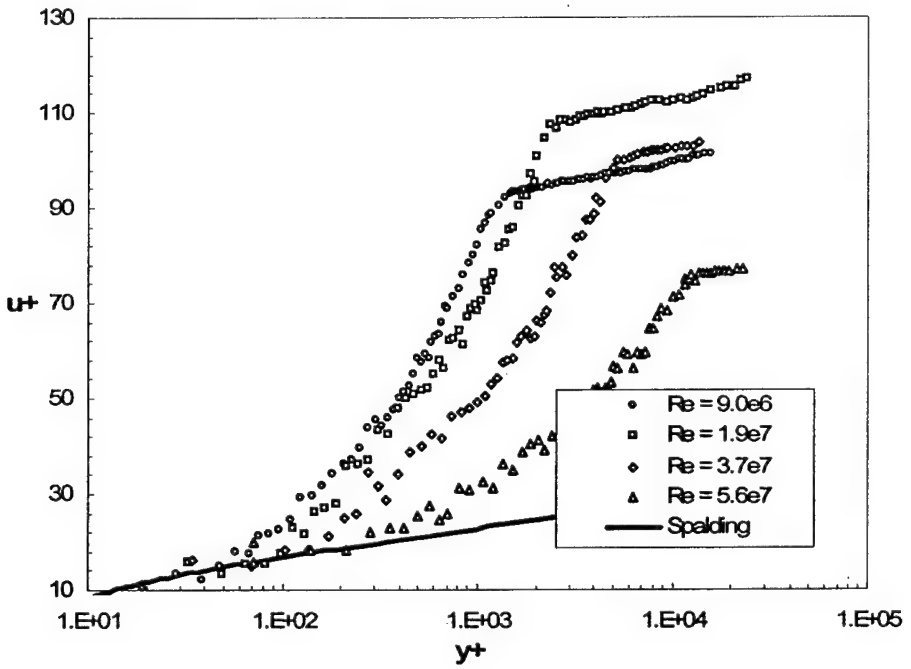

c. x/c = 0.979 suction side.

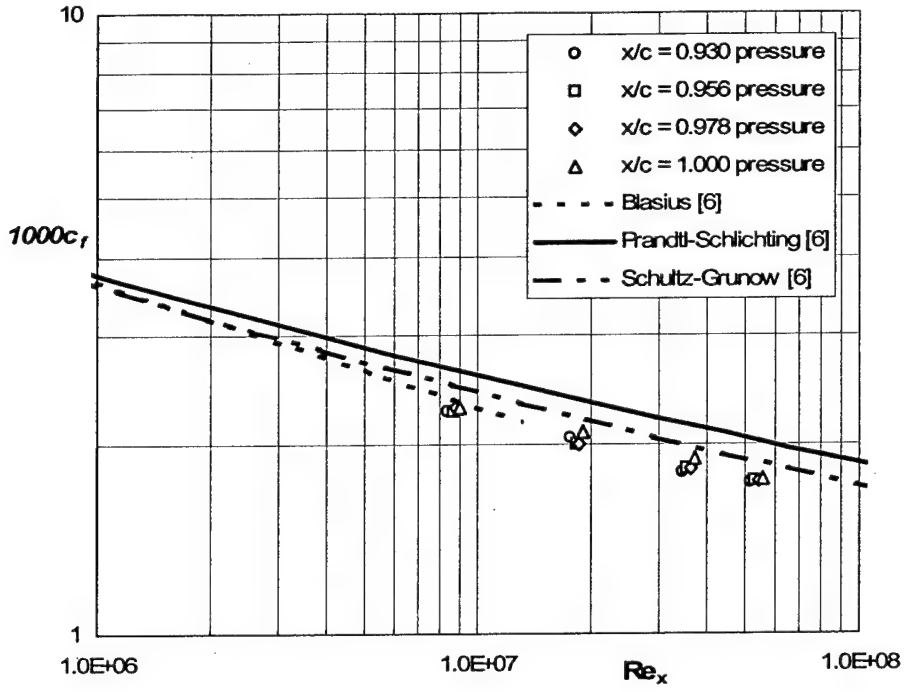

Figure 9. Local skin-friction coefficient computed from pressure-side velocity profiles.

Figure 10. Displacement and momentum thickness versus Reynolds number.

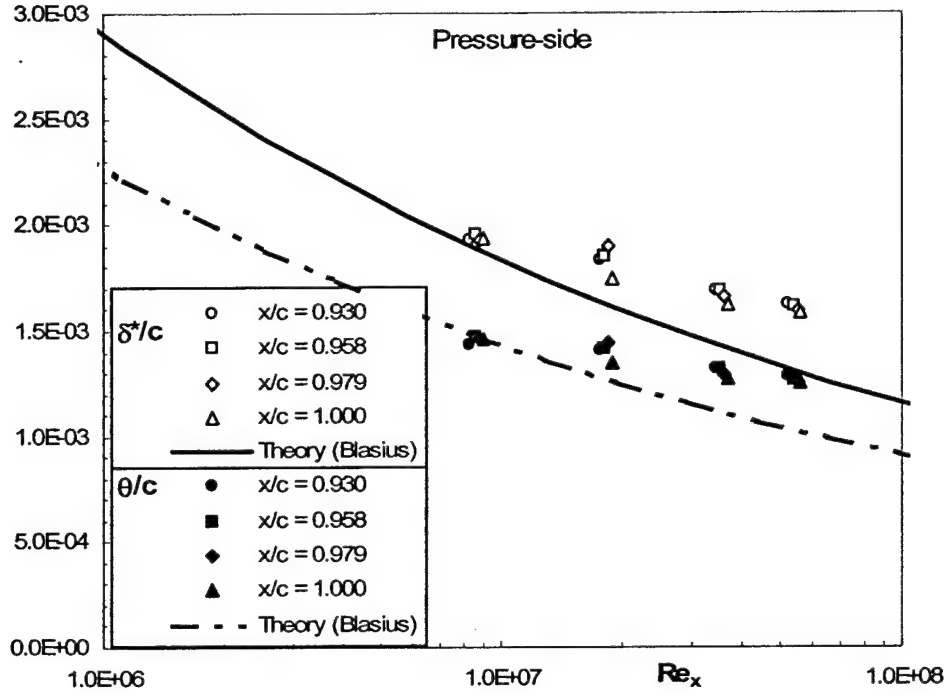

a. Pressure-side displacement and momentum thickness versus Reynolds number.

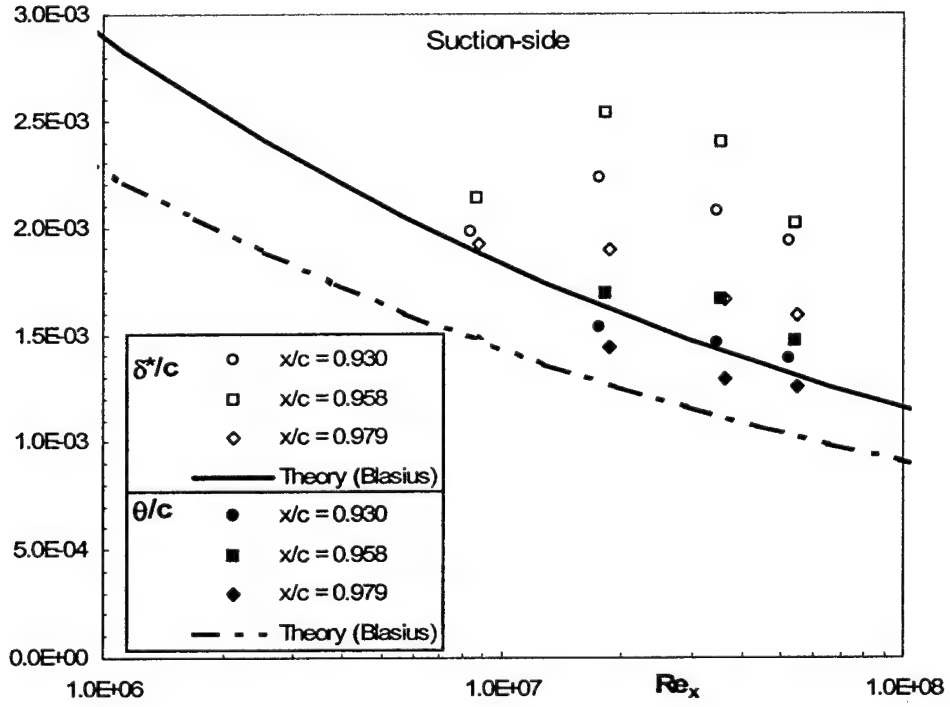

b. Suction-side displacement and momentum thickness versus Reynolds number.

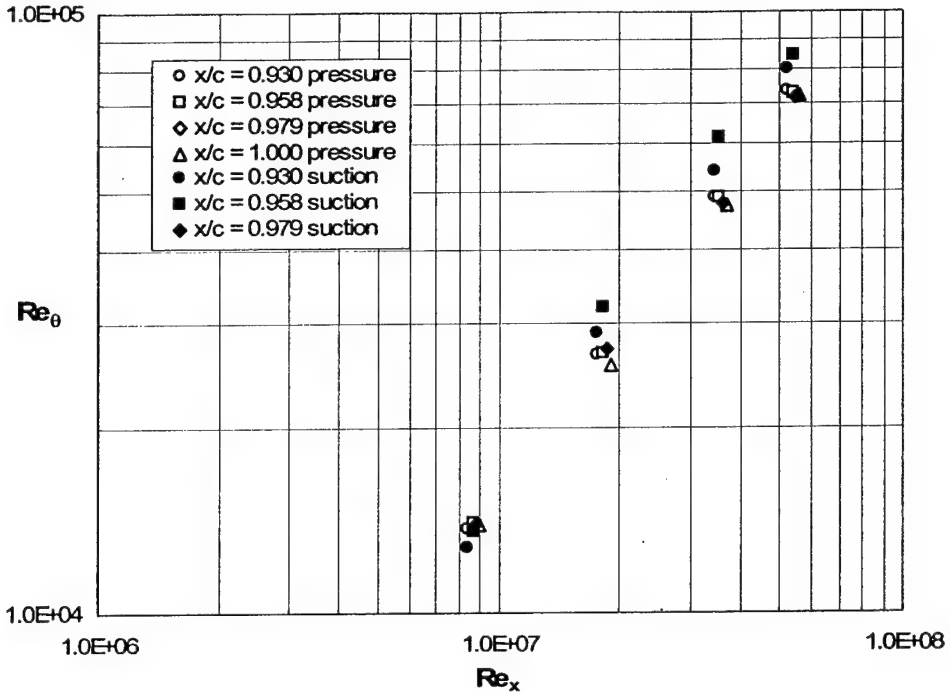

Figure 11. Re_θ versus Re_x

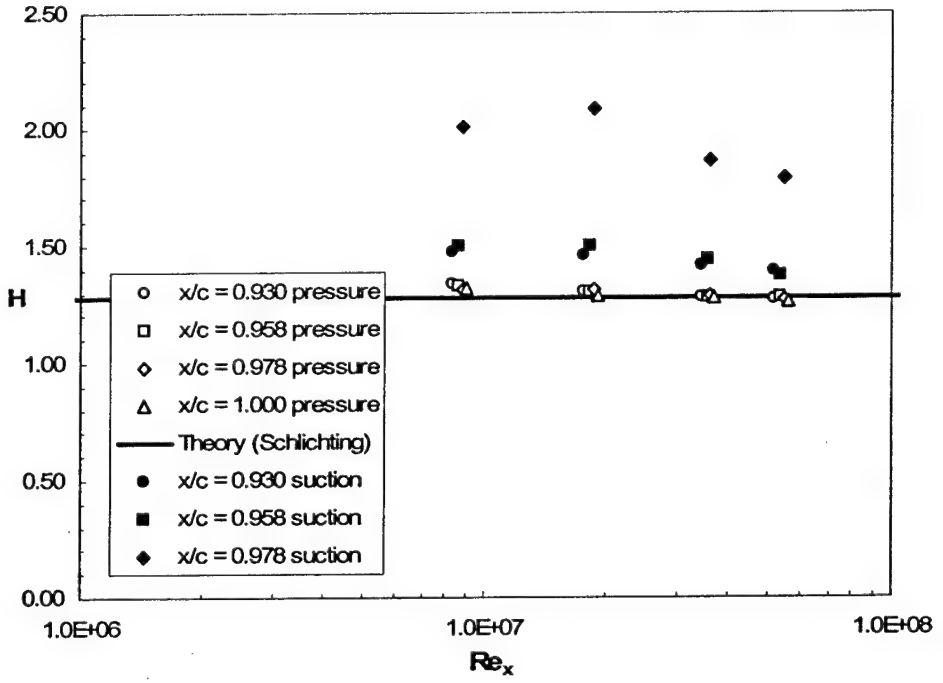

Figure 12. Shape Factor as a function of Reynolds number

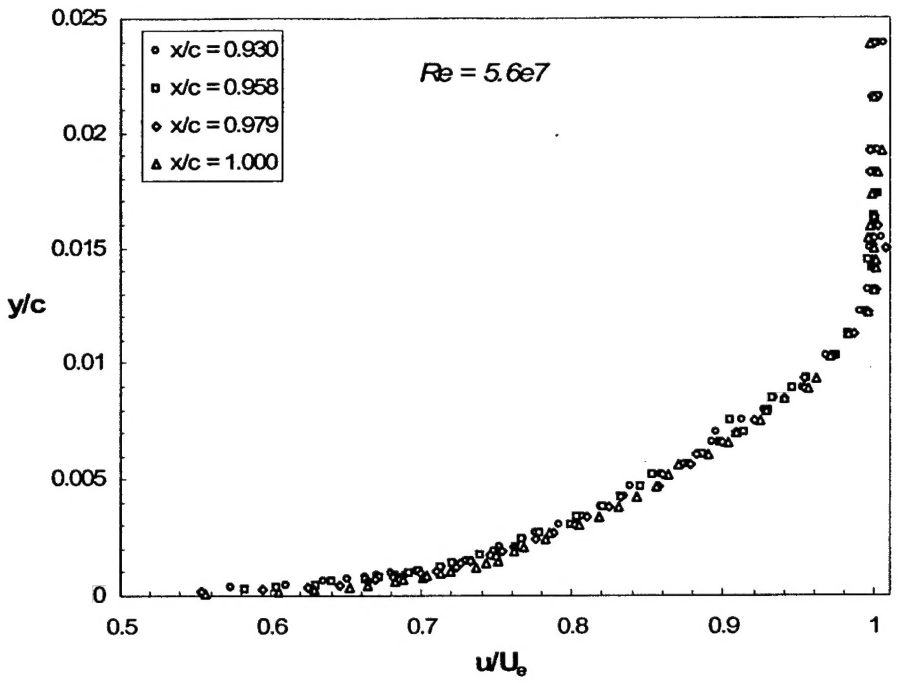

Figure 13. Pressure-side mean axial velocity profiles showing shape similarity.

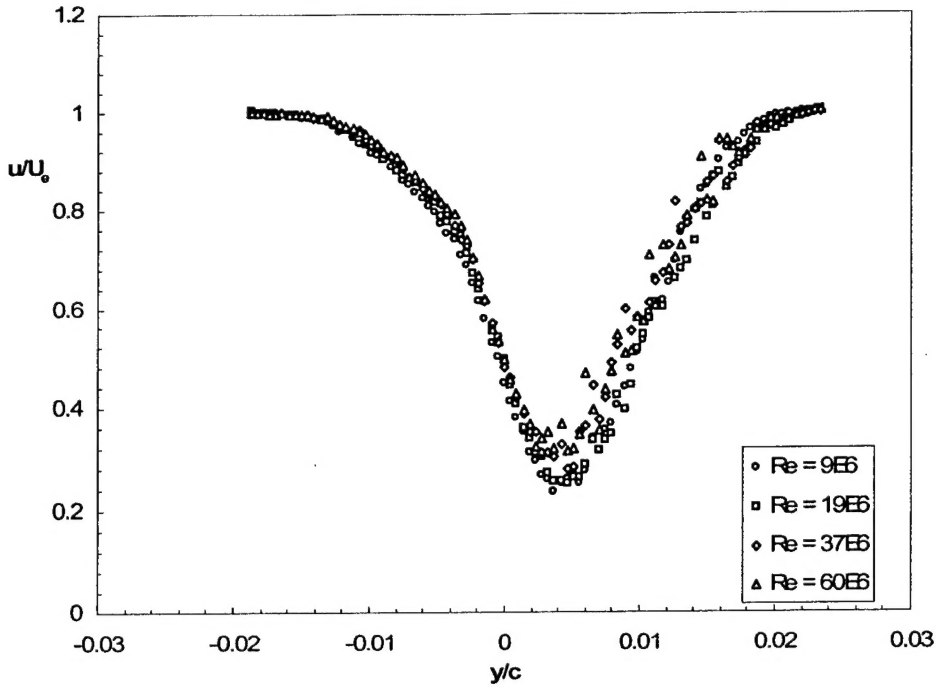

Figure 14. LDV wake measurements taken at x/c = 1.028.

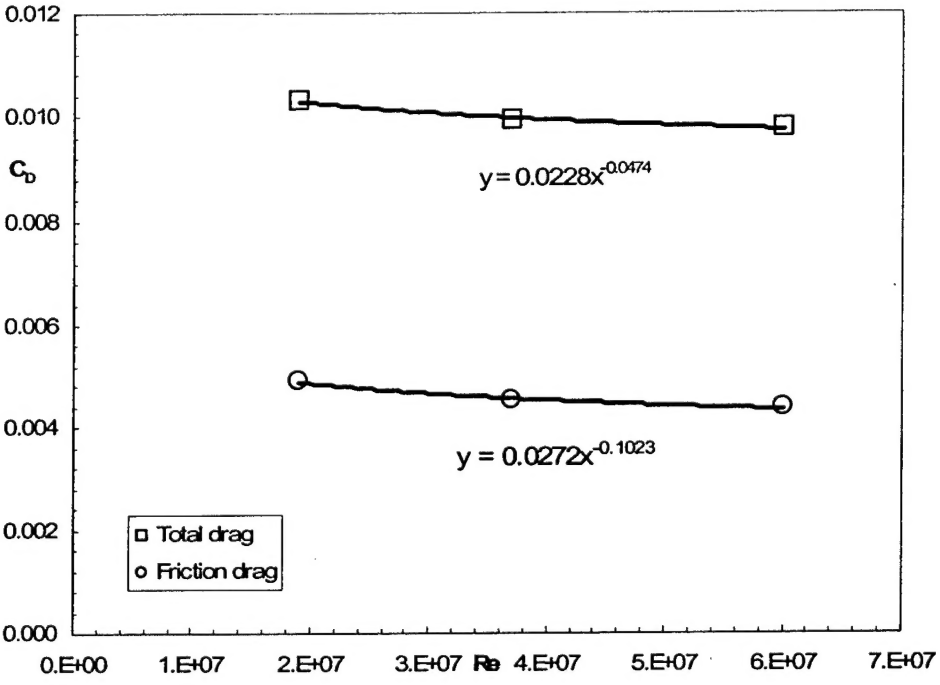

Figure 15. Reynolds number dependence of drag coefficient.

REFERENCES

1. Wark, C. High Reynolds Number Turbulence. ONR Broad Agency Announcement 98-025. October 1998.
2. Etter, R. and Wilson, M., "Testing ship designs in a water tunnel," Mechanical Engineering, October 1993, pp. 74-80.
3. Blanton, J., "Uncertainty estimates of test section pressure and velocity in the Large Cavitation Channel." AIAA Paper No. 95-3079, July 1995.
4. Bourgoyne, D., S. Ceccio, D. Dowling, S. Jessup, J. Park, W. Brewer, R. Pankajakshan. *Hydrofoil turbulent boundary layer separation at high Reynolds numbers.* Presented at the 23rd Symposium on Naval Hydrodynamics. Val De Reuil, France. September 2000.
5. Spalding, D. B. A single Formula for the Law of the Wall. Journal of Applied Mechanics. September 1961, pp. 455-457.
6. Schlichting, H. *Boundary-Layer Theory.* 7th edition. McGraw-Hill, New York, 1968.
7. Hinze, J. O. Turbulence. Second edition. McGraw-Hill, New York, 1975.
8. White, F. Viscous Fluid Flow. McGraw-Hill, New York, 1974.
9. Shen, Y. Private Communications. Summer 2001.

NSWCCD Distribution:

Code	Name
5080	Brown, J. Meyer, R. Boswell, R. Cross, R. Lee, J. Stout
50	Webster, B.
5100	Parks, J. Cutbirth, M.
5060	Walden, D.(12)
5200	Stenson, R.
5400	Szwerc, R. Jessup, S. Shen ,Y. Michael, T. Black, S. Chen B. Gowing, S. Gorski, J. Dai
5500	Applebee, T.
5600	Koh, I.Y. Ammeen, E.

Organization	**Name**
University of Michigan	Ceccio, S.
University of Iowa	Stern, F.
Mississippi State	Whitfield (1) Brewer (3)
Electric Boat	Knight, C.
Bath Iron Works	Cary, C.
Ingalls Ship Building	Weinrich

NAVSEA Distribution:

05H1	Crockett, C Webster, J. Shuman, J.
05H2	Thomas, CMDR Hettema, C.
93R	Dahmer, D.